Using photonic crystal microrings to mitigate Raman-Kerr effects competition for soliton microcomb generation

Zongxing Lin, Dongmei Huang, Zihao Cheng, Wei Wu, P. K. A. Wai, *Fellow*, *IEEE*, Zhe Kang, and Sailing He, *Fellow*, *IEEE*

***Abstract*—In nonlinear microresonators with strong stimulated Raman scattering effect, it is difficult if not impossible to generate Kerr soliton microcombs with a small free spectral range (FSR) (< 100 GHz) due to the competition between the Raman and Kerr effects. In this paper, we overcome this limitation by using odd-period photonic crystal microrings (PCMs). Numerical simulations on the silicon-on-insulator (SOI) PCM show that a small frequency shift (5 GHz) induced by the photonic crystal structure can moderately suppress the Raman effect, such that chaotic microcombs with a small FSR can be generated. With a larger frequency shift (e.g. ≥ 10 GHz), the Raman effect is significantly suppressed, and the soliton microcombs can be generated. For comparison, without the frequency shift, only Raman lasing can be achieved in conventional microrings. To investigate the applicability of the proposed method in other material platforms, we carried out simulations for the aluminium nitride (AlN) PCM. The results are comparable to those obtained on the SOI PCM. Our method opens a new approach for the generation of small FSR Kerr soliton microcombs in microresonators with strong Raman effect, which is important for expanding the available nonlinear platforms and applications such as telecommunications, radio-frequency photonics, and astronomical spectrographs.**

***Index Terms*—Microcombs, Raman effect, free spectral range (FSR), photonic crystal microring (PCM).**

I. Introduction

DUE to the advantages of miniature footprint, broad bandwidth, low pump power threshold, and high coherence, Kerr soliton microcombs have attracted considerable attention in the fields of astronomy, metrology, spectroscopy, communications, etc [1]–[8]. However, some excellent Kerr nonlinear material platforms also possess strong stimulated Raman scattering effect, e.g. silicon, diamond, lithium niobate, and aluminium nitride (AlN) [9]–[14]. The strong Raman effect competes with the Kerr effect, making it difficult if not impossible to generate Kerr soliton microcombs [10]. Two methods have been used to overcome this problem. The first one is to select an appropriate free spectral range (FSR) for the microresonator such that the Raman gain peak is located in the middle of two resonances, which are sufficiently far away from the Raman gain peak [10], [12]. As a result, there is a lower limit on the FSR to ensure that the Raman gain at the two nearby resonances is sufficiently small to avoid competition with the Kerr effect. This FSR lower limit is typically >100 GHz or even terahertz, which is incompatible with the electronic bandwidth. The FSR threshold limits the applications of soliton microcombs in telecommunications [15], [16], radio-frequency photonics [17], and calibration of astronomical spectrographs [18], where a small FSR compatible with the electronic bandwidth is required. Another method is to move the pump to a longer wavelength, such as the mid-infrared, since the Raman gain decreases with increasing pump wavelength [19]. However, expensive or even scarce lasers and amplifiers make this difficult and costly to implement. In addition, a longer pump wavelength also affects the spectral range generated.

Recently, photonic crystal microrings (PCMs) have attracted considerable attention [20]–[26]. By periodically modulating the waveguide width with an even period, a specific resonance can be split into two. The mode number of the splitting resonance and the splitting frequency can be controlled by the period number and modulation amplitude, respectively [20]–[22]. It is also possible to split multiple resonances [21]. The most important features of the PCMs are that the quality factor of the splitting resonances can be maintained and the splitting frequency can be flexibly controlled [21], which is essential for

This work was supported in part by the National Key Research and Development Program of China under Grant 2020YFB1805901; in part by the National Natural Science Foundation of China under Grant 62075188, 62105274; and in part by the Research Grants Council, University Grants Committee of Hong Kong SAR under Grant PolyU15301022. (*Corresponding authors: Dongmei Huang; Sailing He.*)

Zongxing Lin, Zhe Kang, and Sailing He are with the Center for Optical and Electromagnetic Research, National Engineering Research Center for Optical Instruments, Zhejiang University, Hangzhou 310058, China (e-mail: linzongxing@zju.edu.cn; zhe_kang@zju.edu.cn; sailing@zju.edu.cn). Zongxing Lin is also with The Hong Kong Polytechnic University, Hong Kong, SAR, China. Zhe Kang and Sailing He are also with Ningbo Innovation Center, Zhejiang University, Ningbo 315100, China.

Dongmei Huang, Zihao Cheng, and Wei Wu are with Photonics Research Institute, Department of Electrical Engineering, The Hong Kong Polytechnic University, Hong Kong, SAR, China (e-mail: meihk.huang@polyu.edu.hk; zihao.cheng@connect.polyu.hk; wuwei.opt@gmail.com).

P. K. A. Wai is with the Department of Physics, Hong Kong Baptist University, Hong Kong, SAR, China (e-mail: alexwai@hkbu.edu.hk).

Color versions of one or more of the figures in this article are available online at http://ieeexplore.ieee.org

nonlinear photonics. By compensating for the Kerr mismatch between the pulse state and its pump mode through the PCM, spontaneous and deterministic generation of Kerr solitons has been achieved [22]. In [23], the dark-to-bright pulse continuum was accessed and explored by phase-matching with the PCM, which mediates the competition between nonlinearity and normal group velocity dispersion (GVD). With the PCM, the group velocity of the modes near the dielectric band edge can be slowed down by a factor of 10 compared to conventional microring modes while supporting high Q values. In addition, by using the photonic crystal defect modes, the mode volume can be reduced by more than 10 times compared to conventional microrings [24].

In this paper, we use the odd-period PCM to mitigate the Raman-Kerr effect competition for the generation of soliton microcombs with small FSR (<100 GHz). In Section II, we illustrate the principle of even-period and odd-period PCMs and how the Raman gain is suppressed in the odd-period PCMs. In Sections III and IV, we investigate the feasibility of the proposed method by carrying out simulations using the Ikeda map equations and coupled Ikeda map equations on the silicon-on-insulator (SOI) and AlN PCMs, respectively. The simulation results on the SOI and AlN platforms show that the Raman effect can be strongly suppressed and the Kerr soliton microcombs can be generated at small FSR in odd-period PCMs. Section V concludes the paper.

II. Principle

A. PCMs with even and odd periods

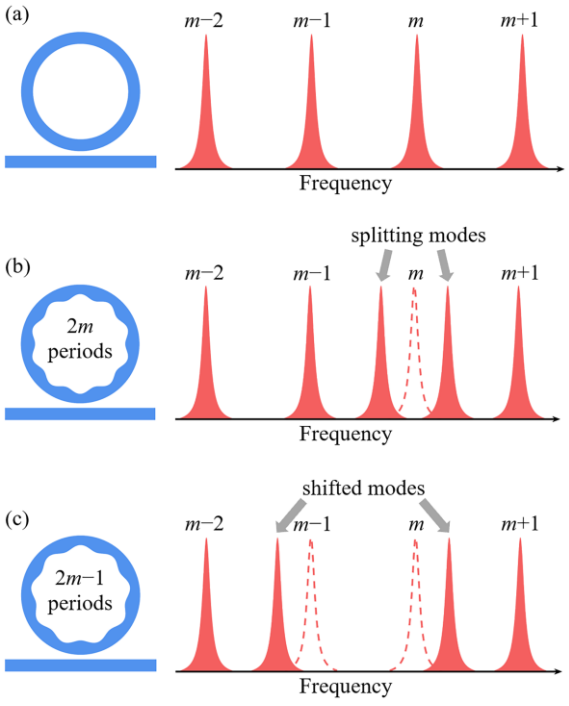

Fig. 1. (a) Microring (blue) and its resonances (red). (b) Even-period PCM (blue) and its resonances (red). (c) Odd-period PCM (blue) and its resonances (red). The red dashed curves represent the resonances of the microring without width modulation.

A microring, as shown in Fig. 1(a), has many resonances. The mode number m of the resonances is defined by neffL = mλ, where neff is the effective refractive index of the transverse mode, L is the cavity length of the microring, and λ is the wavelength. A PCM is formed by periodically modulating the waveguide width of the microring as $w = w_0 + w_1\cos(n\varphi)$ [21], where, w_0 is the initial waveguide width, w is the waveguide width after modulation, w_1 is the modulation amplitude, φ and n are the azimuthal angle and the modulation period corresponding to a single round trip.

If n is even (e.g. $n = 2m$), the photonic crystal structure will generate a band gap centered on the resonance with mode number m, which degenerates this resonance and splits it into two resonances [21], [22], [24], [25]. Furthermore, the band gap pushes the splitting resonances away from each other with a splitting frequency [21], as shown in Fig. 1(b). The magnitude of the splitting frequency is determined by the modulation amplitude w_1 (a larger w_1 would induce a larger splitting frequency). If n is odd (e.g. $n = 2m–1$), the photonic crystal structure will generate a band gap in the middle of the resonances with mode numbers $m–1$ and m. The generated band gap would push these two resonances away from each other with a frequency shift, as shown in Fig. 1(c). The magnitude of the frequency shift is also determined by w_1. A larger modulation amplitude w_1 would induce a larger frequency shift. We therefore focus our study on odd-period PCM, as its effect of pushing the two resonances away from each other can be better exploited to suppress the Raman effect.

B. Suppression of the Raman gain using odd-period PCM

Figure 2 shows the relative position of the resonances (red) and the Raman gain spectrum (blue). To suppress the Raman effect at a given pump wavelength, we can choose an appropriate FSR to locate the Raman gain peak in the middle of two resonances and make these two resonances sufficiently far from the Raman gain peak [10]. However, to ensure that the Kerr effect is dominant, the FSR of the microring should be sufficiently large. In this case, the Raman gain at the two resonances near the Raman gain peak would be sufficiently small to ensure the generation of Kerr soliton microcombs. Therefore, microrings with small FSRs will find it difficult if not impossible to generate Kerr soliton microcombs due to the significant overlap between Raman gain and resonances.

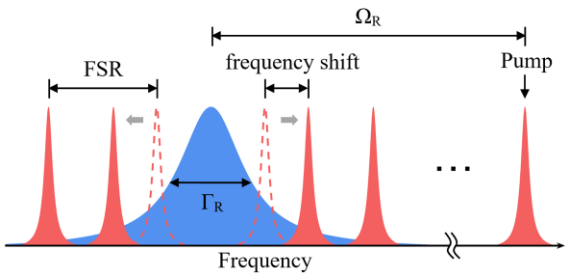

Fig. 2. The relative position of the resonances (red) and the Raman gain spectrum (blue). The red dashed curves represent the resonances of the microring without width modulation. Γ_R is the Raman gain linewidth and Ω_R is the Raman frequency shift.

To reduce the FSR limitation caused by the competition between the Raman and Kerr effects, we propose to use odd-period PCMs to generate Kerr soliton microcombs. By modulating the waveguide width of the microring with a selected odd period, we can shift the two resonances close to the Raman gain peak away from each other, as shown in Fig. 2. Since the frequency shift can be controlled by the modulation amplitude w_1, the Raman gain at the two resonances near the Raman gain peak can be controlled and reduced. This reduces the FSR constraint caused by the Raman effect on the microcombs, thus making it possible to generate Kerr soliton microcombs at small FSRs.

III. Simulations And Analyses On The SOI PCM

We first carried out simulations and analyses on the SOI PCM to show that the proposed PCM configuration can mitigate the Raman-Kerr effect competition for the generation of Kerr soliton microcombs. The SOI platform has the advantages of high index contrast, high nonlinear coefficient, compact footprint, and compatibility with complementary metal oxide semiconductor (CMOS) fabrication [27]–[29]. The pump wavelength is set at 3100 nm such that the multiphoton absorption and free carrier absorption in silicon can be neglected. The nonlinear refractive index of the silicon is $n_2 = 3\times10^{-18}$ m^2/w at 3100 nm. The Raman gain spectrum of silicon can be approximated as a Lorentz function with Raman frequency shift $\Omega_R = 15.6$ THz and Raman gain linewidth $\Gamma_R = 105$ GHz. The Raman gain peak of silicon is $g_R = 3.05$ cm/GW at 3100 nm [10]. Fig. 2(a) shows the cross-section of the SOI microring with silicon dioxide (SiO_2) cladding. The waveguide parameters are set at $w_{si} = 1500$ nm and $h_{si} = 400$ nm to ensure a small and flat anomalous dispersion near the pump wavelength, as shown in Fig. 2(b). The transmission loss of the waveguide is chosen to be 0.7 dB/cm according to the recent experimental results [10], [29]. The FSR of the microring is chosen as 77.8 GHz to ensure that the Raman gain peak is located in the middle of two resonances (15.6 THz/77.8 GHz ≈ 200.5). At this FSR, the Raman gain at the two resonances close to the Raman gain peak is more than twice the Kerr gain.

A. Simulations on the microring without width modulation

For comparison, we first performed simulations on a conventional microring without width modulation. The simulations are based on the Ikeda map equations [10], [30],

$$\frac{\partial A}{\partial z} = -\frac{\alpha_i}{2}A - j\frac{T_R}{L}\sum_{\mu} D_{int}(\mu)e^{-j\mu\varphi}\widetilde{A} + \frac{j\gamma\hbar\omega_0}{T_R}\left(1+\frac{j}{\omega_0}\frac{\partial}{\partial t}\right)\left\{A(z,t)\left[R(t)\otimes\left|A(z,t-t')\right|^2\right]\right\}, \quad (1)$$

$$A^{(k+1)}(0,t) = \sqrt{\theta}A_{in} + \sqrt{1-\theta}A^{(k)}(L,t)e^{j\phi}, \quad (2)$$

where A is the slowly varying envelope of the field normalized by the photon number and $\widetilde{A}$ is the Fourier transform of A. j is the imaginary number, z is the distance on the microring, and t is the fast time corresponding to the time domain. α_i is the linear transmission loss and $T_R = 1/\text{FSR}$ is the round-trip time. μ is the azimuthal mode number referenced to the pumped mode. D_{int} is the integrated dispersion of the microring and is defined as $D_{int} = \omega_{res}-(\omega_0+D_1\mu)$, where ω_{res} is the angular frequency of the resonances, ω_0 is the angular frequency of the pump, and D_1 is defined as $D_1/2\pi = \text{FSR}$. $\gamma = (n_2\omega_0)/(cA_{eff})$ is the nonlinear parameter, where c is the speed of light in vacuum and A_{eff} is the effective mode area. $\hbar$ is the reduced Planck constant and ω_0 is the angular frequency of the pump. $R(t) = (1-f_R)\delta(t) + f_R h_R(t)$ is the response function, where f_R is the Raman contribution and $h_R(t)$ is the Raman response function. f_R and $h_R(t)$ can be calculated from the Raman gain spectrum [31]–[33]. The symbol "⊗" represents the convolution calculation. k is the round-trip number, θ is the power coupling ratio, and A_{in} is the pump field normalized by the photon number. ϕ is the linear phase accumulated by the intracavity field with respect to the pump field in a round trip.

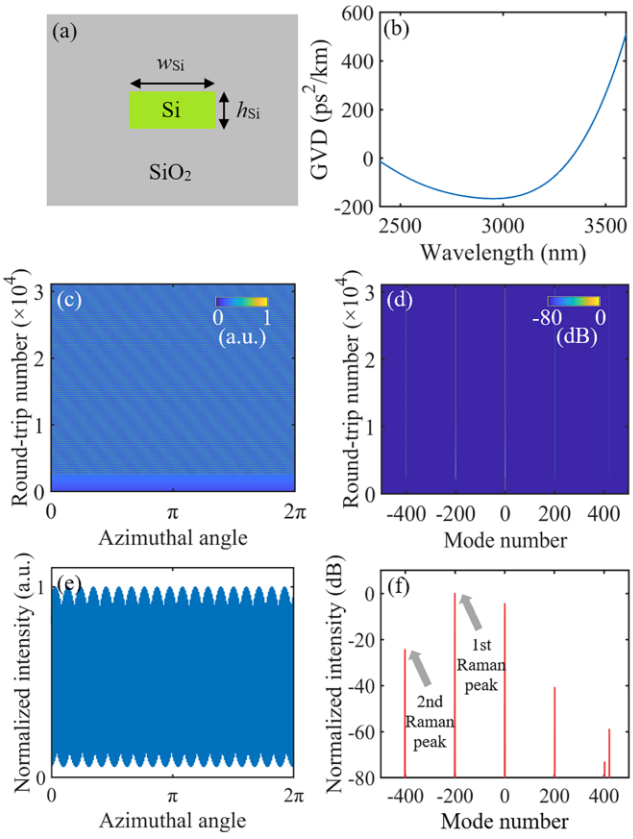

Fig. 3. (a) Cross section of the SOI microring. (b) GVD of the SOI microring with $w_{si} = 1500$ nm and $h_{si} = 400$ nm. Simulated (c) temporal and (d) spectral evolution profiles of the intracavity field in a conventional microring without width modulation. The pump power is set at 30 mW. Instantaneous (e) temporal and (f) spectral profiles of (c) and (d) at the final roundtrip.

Figures 3(c) and 3(d) show the simulated temporal and spectral evolution profiles in a conventional microring without width modulation, where the pump power is set at 30 mW. After ~2.5×10^3 roundtrips, the temporal profile becomes rapidly oscillating. At the same time, the spectral profile shows multiple Raman lasing, which manifests as multiple discrete

resonant frequencies with frequency intervals equal to the Raman frequency shift. This means that the Raman effect dominates over the Kerr effect due to the large Raman gain caused by the small FSR. The first-order Raman peak is located at $\mu \approx -200$ (about 15.6 THz away from the pump). The second-order Raman peak located at $\mu \approx -400$ also appears due to the strong first-order Raman peak. In addition, the generated first- and second-order Raman peaks can interact with the pump to generate two new frequencies located at $\mu \approx 200$ and 400 due to four-wave mixing (FWM). Figs. 3(e) and 3(f) show the instantaneous temporal and spectral profiles, respectively, at the final roundtrip, where fast oscillations in the temporal profile and multiple discrete resonant frequencies in the spectral profile are observed.

B. Simulations on the odd-period PCM

We then performed simulations on the odd-period PCM with the same FSR (77.8 GHz). Due to the reflection induced by the photonic crystal structure, optical fields exist in both directions inside the PCM and there are both linear and nonlinear couplings between them. Therefore, the simulations were performed based on the coupled Ikeda map equations [10], [26], [30],

$$\frac{\partial A_{\uparrow}}{\partial z} = -\frac{\alpha_i}{2}A_{\uparrow} - j\frac{T_R}{L}\sum_{\mu} D_{int}(\mu)e^{-j\mu\varphi}\widetilde{A_{\uparrow}} + j\frac{T_R}{L}\sum_{\mu} J(\mu)e^{-j\mu\varphi}\widetilde{A_{\downarrow}} + \frac{2j\gamma\hbar\omega_0}{T_R}\int_{-\pi}^{\pi}\frac{|A_{\downarrow}|^2}{2\pi}d\varphi\, A_{\uparrow} + \frac{j\gamma\hbar\omega_0}{T_R}\left(1+\frac{j}{\omega_0}\frac{\partial}{\partial t}\right)\left\{A_{\uparrow}(z,t)\left[R(t)\otimes|A_{\uparrow}(z,t-t')|^2\right]\right\}, \quad (3)$$

$$\frac{\partial A_{\downarrow}}{\partial z} = -\frac{\alpha_i}{2}A_{\downarrow} - j\frac{T_R}{L}\sum_{\mu} D_{int}(\mu)e^{-j\mu\varphi}\widetilde{A_{\downarrow}} + j\frac{T_R}{L}\sum_{\mu} J(\mu)e^{-j\mu\varphi}\widetilde{A_{\uparrow}} + \frac{2j\gamma\hbar\omega_0}{T_R}\int_{-\pi}^{\pi}\frac{|A_{\uparrow}|^2}{2\pi}d\varphi\, A_{\downarrow} + \frac{j\gamma\hbar\omega_0}{T_R}\left(1+\frac{j}{\omega_0}\frac{\partial}{\partial t}\right)\left\{A_{\downarrow}(z,t)\left[R(t)\otimes|A_{\downarrow}(z,t-t')|^2\right]\right\}, \quad (4)$$

$$A_{\uparrow}^{(k+1)}(0,t) = \sqrt{\theta}A_{in} + \sqrt{1-\theta}A_{\uparrow}^{(k)}(L,t)e^{j\phi}, \quad (5)$$

$$A_{\downarrow}^{(k+1)}(0,t) = \sqrt{1-\theta}A_{\downarrow}^{(k)}(L,t)e^{j\phi}. \quad (6)$$

Here, $A_{\uparrow}$ and $A_{\downarrow}$ are the slowly varying envelopes of the counter-clockwise (CCW) field (in the same direction as the pump) and clockwise (CW) field (in the opposite direction to the pump), respectively, normalized by the photon number. $\widetilde{A_{\uparrow}}$ and $\widetilde{A_{\downarrow}}$ are the Fourier transform of $A_{\uparrow}$ and $A_{\downarrow}$, respectively. The linear coupling induced by the photonic crystal structure and the nonlinear coupling induced by the cross-phase modulation (XPM) between the fields in two directions have been included, corresponding to the third and fourth terms on the right hand sides of Eqs. (3) and (4), respectively. J is the linear coupling parameter and is determined by the frequency shift [26].

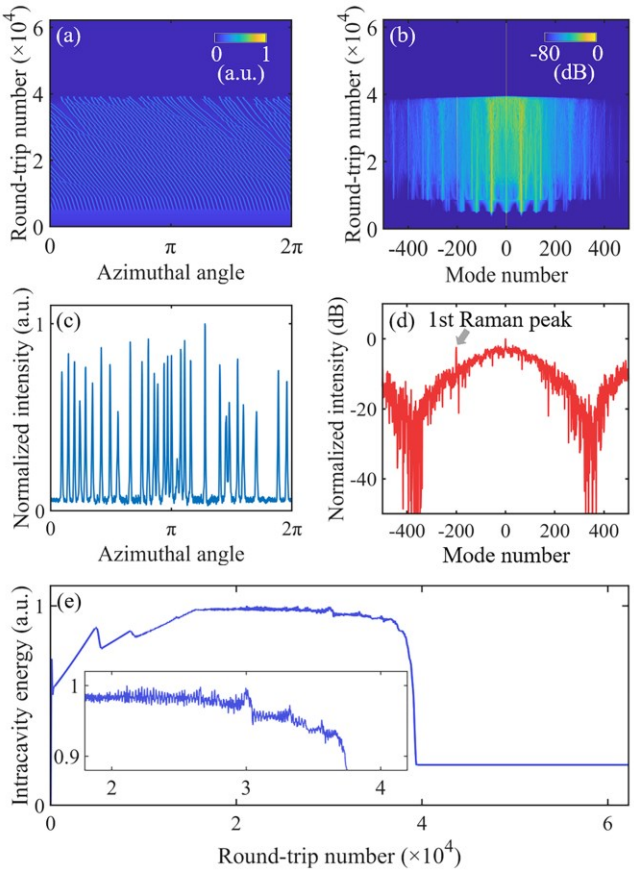

Fig. 4. Simulated (a) temporal and (b) spectral evolution profiles of the CCW field in an odd-period PCM. The pump power and the frequency shift are set at 70 mW and 5 GHz, respectively. Instantaneous (c) temporal and (d) spectral profiles of the CCW field before leaving the soliton existence region. (e) Simulated normalized intracavity energy evolution profile of the CCW field corresponding to (a) and (b). The inset is the zoom-in view of the oscillation region.

The frequency shift was first set at 5 GHz. Figs. 4(a) and 4(b) show the simulated temporal and spectral evolution profiles of the CCW field in an odd-period PCM, respectively, with the pump power set at 70 mW. Compared to Figs. 3(a) and 3(b), the modulation instability (MI) and chaotic states can be reached at the same FSR due to the moderate suppression of the Raman effect. However, the Raman effect is still sufficiently strong so that the soliton states remain difficult to reach. Figs. 4(c) and 4(d) show the instantaneous temporal and spectral profiles of the CCW field before leaving the soliton region (the round-trip number is about 3.9×10^4). We find that both the temporal and spectral profiles are chaotic. We also see that the Raman peak at $\mu \approx -200$ is still very strong, preventing the generation of soliton states. Fig. 4(e) shows the normalized intracavity energy evolution profile of the CCW field corresponding to Figs. 4(a) and 4(b), where no soliton steps exist. The inset in Fig. 4(e) is the zoom-in view of the oscillation region, showing the competition between the Raman and Kerr effects.

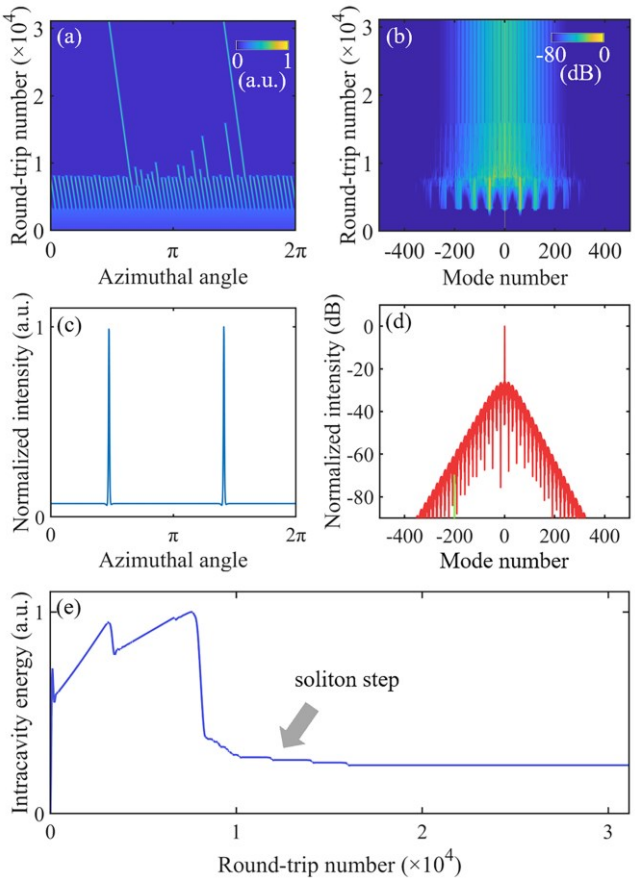

Fig. 5. Simulated (a) temporal and (b) spectral evolution profiles of the CCW field in an odd-period PCM. The pump power and the frequency shift are set at 70 mW and 10 GHz, respectively. Instantaneous (c) temporal and (d) spectral profiles of (a) and (b) at the final roundtrip. The green curve in (d) is the instantaneous spectral profile of the CW field at the final roundtrip. (e) Simulated normalized intracavity energy evolution profile of the CCW field corresponding to (a) and (b).

We then chose the frequency shift as 10 GHz, where the Raman effect is significantly suppressed compared to that of the frequency shift of 5 GHz. Figs. 5(a) and 5(b) show the simulated temporal and spectral evolution profiles of the CCW field, respectively, with the pump power is set at 70 mW. For the temporal evolution profiles, the CCW field evolves from the continuous wave, first to the MI state, then to the multiple soliton state, and finally to the two-soliton state. For the spectral evolution profiles, the primary comb is first generated in the MI state. Then the spectral profile is modulated with a smooth envelope in the multiple soliton and two-soliton states. Figs. 5(c) and 5(d) show the instantaneous temporal and spectral profiles, respectively, at the final roundtrip. The temporal profile manifests as two solitons and the spectral profile shows a modulated spectrum with a smooth envelope. In addition, Fig. 5(d) also shows the full instantaneous spectral profile of the CW field (green curve) caused by the linear coupling, which has a similar intensity to the CCW field at $\mu \approx -200$. Fig. 5(e) shows the normalized intracavity energy evolution profile of the CCW field. The soliton step is clearly shown, indicating that the soliton states are reached.

IV. Simulations And Analyses On The AlN PCM

We now carried out simulations on the AlN PCM to show that the proposed PCM configuration can mitigate the Raman-Kerr effect competition for the generation of Kerr soliton microcombs in other material platforms. The AlN material exhibits both second and third order nonlinear effects as well as an enormous bandgap, thus making it ideal for nonlinear optical interactions with negligible multi-photon absorption [13], [34]–[36]. The second order nonlinear effect of AlN is essential for chip-based self-referencing with an *f*-2*f* interferometer, making fully integrated self-locked microcombs feasible [13]. The pump wavelength is set at 1550 nm, which is important for optical communications and devices at this wavelength are readily available. The nonlinear index coefficient of AlN is $n_2 = 2.3\times10^{-19}$ m^2/w at 1550 nm. The Raman gain spectrum of AlN can be expressed as a Lorentz function with Raman frequency shift $\Omega_R = 18.3$ THz and Raman gain linewidth $\Gamma_R = 138$ GHz. The Raman gain peak of AlN is $g_R = 0.45$ cm/GW at 1550 nm [13], [14]. Fig. 6(a) shows the cross-section of the AlN microring. Based on the existing growth of single-crystalline AlN films and fabrication of AlN waveguide, the AlN film sits on the *c*-plane (0001) of sapphire with SiO_2 cladding [13], [14], [36]. The waveguide parameters are set at $w_{AlN} = 1500$ nm, $h_{AlN} = 830$ nm, and $h_{slab} = 400$ nm to ensure a small and flat anomalous dispersion near the pump, as shown in Fig. 6(b). The transmission loss of the waveguide is chosen at 0.1 dB/cm according to recent experimental results [13], [36]. The FSR of the microring is chosen as 80.8 GHz to ensure that the Raman gain peak is located in the middle of two resonances (18.3 THz/80.8 GHz ≈ 226.5). For this FSR, the Raman gain at the two resonances near the Raman gain peak is more than twice the Kerr gain.

A. Simulations on the microring without width modulation

For comparison, we first performed simulations on a conventional microring without width modulation. The simulations are based on Eqs. (1) and (2). The simulated results are similar to those obtained on the SOI platform. Figs. 6(c) and 6(d) show the simulated temporal and spectral evolution profiles in a conventional microring without width modulation, where the pump power is set at 200 mW. The temporal profile becomes rapidly oscillating and the spectral profile shows multiple discrete resonant frequencies after about 6.7×10^3 roundtrips, indicating that the Raman effect dominates over the Kerr effect. The first and second order Raman peaks appear at $\mu \approx -226$ and -452 due to the strong Raman effect and generate two new frequencies located at $\mu \approx 226$ and 452 by interacting with the pump through FWM. Figs. 6(e) and 6(f) show the instantaneous temporal and spectral profiles at the final roundtrip, showing the fast oscillation in the temporal profile and multiple discrete resonant frequencies in the spectral profile.

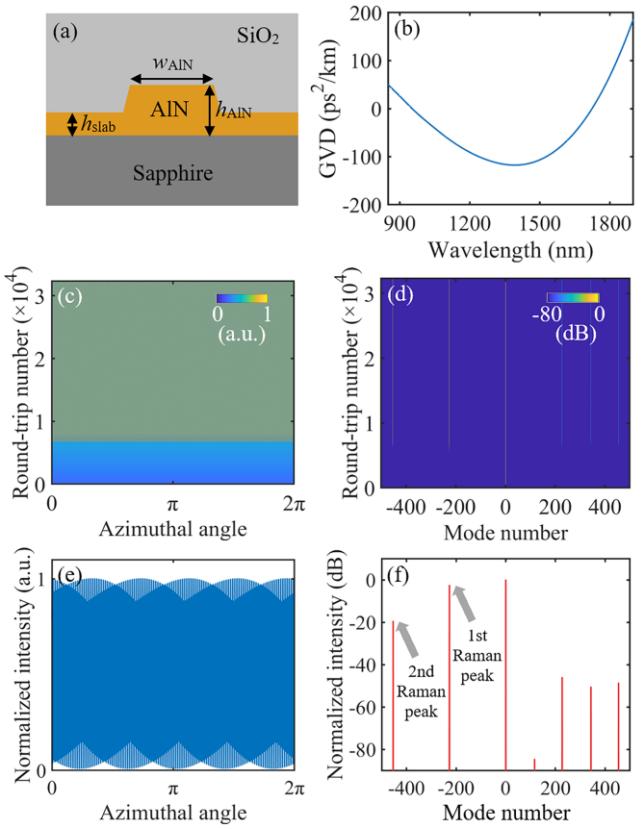

Fig. 6. (a) Cross section of the AlN microring. (b) GVD of the AlN microring with w_{AlN} = 1500 nm, h_{AlN} = 830 nm, and h_{slab} = 400 nm. Simulated (c) temporal and (d) spectral evolution profiles of the intracavity field in a conventional microring without width modulation. The pump power is set at 200 mW. Instantaneous (e) temporal and (f) spectral profiles of (c) and (d) at the final roundtrip.

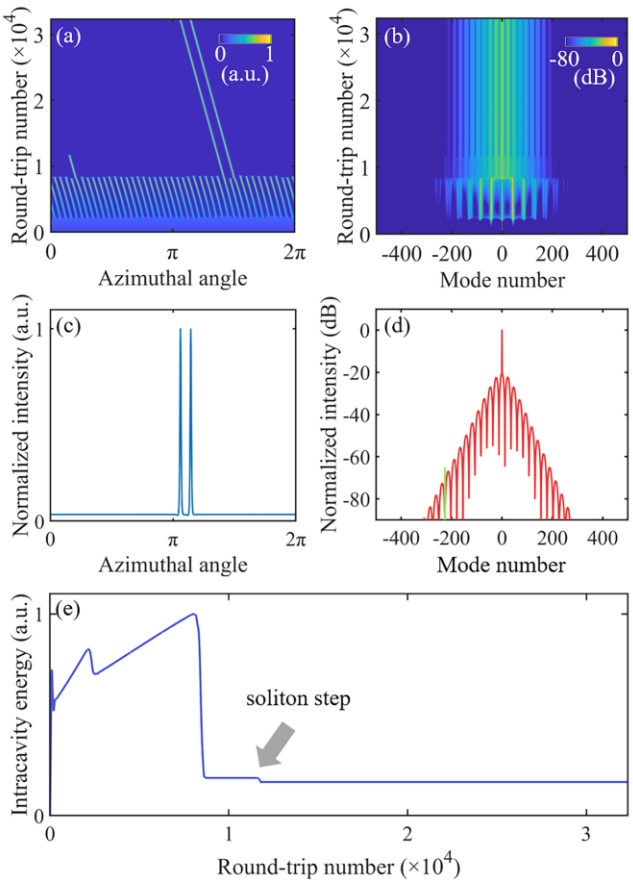

Fig. 7. Simulated (a) temporal and (b) spectral evolution profiles of the CCW field in an odd-period PCM. The pump power and the frequency shift are set at 600 mW and 10 GHz, respectively. Instantaneous (c) temporal and (d) spectral profiles of (a) and (b) at the final roundtrip. The green curve in (d) is the instantaneous spectral profile of the CW field at the final roundtrip. (e) Simulated normalized intracavity energy evolution profile of the CCW field corresponding to (a) and (b).

B. Simulations on the odd-period PCM

We then carried out simulations on the odd-period PCM. The simulations are also based on Eqs. (3)-(6) and the frequency shift is set at 10 GHz. Figs. 7(a) and 7(b) show the simulated temporal and spectral evolution profiles of the CCW field in an odd-period PCM, respectively, where the pump power is set at 600 mW. Figs. 7(c) and 7(d) show the temporal evolution profile finally evolves to the two-soliton state and the spectral profile modulated with a smooth envelope, respectively. Fig. 7(d) also shows the full instantaneous spectral profile of the CW field (green curve) caused by the linear coupling, which has a a similar intensity to the CCW field at $\mu \approx -226$. Fig. 7(e) shows the normalized intracavity energy evolution profile of the CCW field. The soliton step is clearly shown, indicating that the soliton states are reached.

V. Conclusion

In conclusion, we show that by using the odd-period PCM, we can reduce the FSR constraint on the microcomb generation caused by the Raman effect. The PCM can shift the two resonances near the Raman gain peak away from each other, which reduces the Raman gain at these two resonances and allows the Kerr effect to dominate over the Raman effect. Simulations show that the proposed odd-period PCM approach can be used on both the SOI and AlN platforms to generate Kerr soliton microcombs at a small FSR (< 100 GHz). The use of odd-period PCM can be extended to other nonlinear platforms with strong Raman effect, such as diamond and thin-film lithium-niobate-on-insulator (LNOI) [11], [12], which are promising for applications such as telecommunications, radio-frequency photonics, and calibration of astronomical spectrographs.

ACKNOWLEDGMENT

The authors declare that they have no conflicts of interest related to this work.

REFERENCES

[1] T. J. Kippenberg, A. L. Gaeta, M. Lipson and M. L. Gorodetsky, "Dissipative Kerr solitons in optical microresonators," *Science*, vol. 361, no. 567, pp. 1-11, Aug. 2018, doi: 10.1126/science.aan8083.

[2] T. Tanabe, S. Fujii and R. Suzuki, "Review on microresonator frequency combs," *Jpn. J. Appl. Phys.*, vol. 58, no. SJ0801, pp. 1-9, Jul. 2019, doi: 10.7567/1347-4065/ab2aca.

[3] W. Wang, L. Wang and W. Zhang, "Advances in soliton microcomb generation," *Adv. photonics*, vol. 2, no. 3, pp. 1-27, Jun. 2020, doi: 10.1117/1.AP.2.3.034001.

[4] A. L. Gaeta, M. Lipson and T. J. Kippenberg, "Photonic-chip-based frequency combs," *Nat. Photonics*, vol. 13, pp. 158-169, Feb. 2019, doi: 10.1038/s41566-019-0358-x.

[5] A. Pasquazi, et al., "Micro-combs: A novel generation of optical sources," *Phys. Rep.*, vol. 729, pp. 1-81, Jan. 2018, doi: 10.1016/j.physrep.2017.08.004.

[6] H. Zhang, et al., "Coherent optical frequency combs: From principles to applications," *J. Electron. Sci. Technol.*, vol. 20, no. 2, pp. 1-19, Jun. 2022, doi: 10.1016/j.jnlest.2022.100157.

[7] L. Chang, S. Liu and J. E. Bowers, "Integrated optical frequency comb technologies," *Nat. Photonics*, vol. 16, pp. 95-108, Feb. 2022, doi: 10.1038/s41566-021-00945-1.

[8] M. Tan, X. Xu, J. Wu, R. Morandotti, A. Mitchell and D. J. Moss, "RF and microwave photonic temporal signal processing with Kerr micro-combs," *ADV PHYS-X*, vol. 6, no. 1, pp. 1-46, Nov. 2020, doi: 10.1080/23746149.2020.1838946.

[9] A. G. Griffith, et al., "Coherent mid-infrared frequency combs in silicon-microresonators in the presence of Raman effects," *Opt. Express*, vol. 24, no. 12, pp. 13044-13050, Jun. 2016, doi: 10.1364/OE.24.013044.

[10] Y. Okawachi, et al., "Competition between Raman and Kerr effects in microresonator comb generation," *Opt. Lett.*, vol. 42, no. 14, pp. 2786-2789, Jul. 2017, doi: 10.1364/OL.42.002786.

[11] C. Wang, M. Zhang, M. Yu, R. Zhu, H. Hu and M. Loncar, "Monolithic lithium niobate photonic circuits for Kerr frequency comb generation and modulation," *Nat. Commun.*, vol. 10, no. 978, pp. 1-6, Feb. 2019, doi: 10.1038/s41467-019-08969-6.

[12] M. Yu, et al., "Raman lasing and soliton mode-locking in lithium niobate microresonators," *Light Sci. Appl.*, vol. 9, no. 9, pp. 1-7, Jan. 2020, doi: 10.1038/s41377-020-0246-7.

[13] X. Liu, Z. Gong, A. W. Bruch, J. B. Surya, J. Lu and H. X. Tang, "Aluminum nitride nanophotonics for beyond-octave soliton microcomb generation and self-referencing," *Nat. Commun.*, vol. 12, no. 5428, pp. 1-7, Sep. 2021, doi: 10.1038/s41467-021-25751-9.

[14] X. Liu, et al., "Integrated continuous-wave aluminum nitride Raman laser," *Optica*, vol. 4, no. 8, pp. 893-896, Aug. 2017, doi: 10.1364/OPTICA.4.000893.

[15] A. Fülöp, M. Mazur, A. Lorences-Riesgo, Ó. B. Helgason, P. Wang, Y. Xuan, D. E. Leaird, M. Qi, P. A. Andrekson, A. M. Weiner, and V. Torres-Company, "High-order coherent communications using mode-locked dark-pulse Kerr combs from microresonators," *Nat. Commun.,* vol. 9, no. 1598, pp. 1-8, Apr. 2018, doi: 10.1038/s41467-018-04046-6.

[16] M. Mazur, M. Suh, A. Fulop, J. Schroder, V. Torres-Company, M. Karlsson, K. J. Vahala, and P. A. Andrekson, "High Spectral Efficiency Coherent Superchannel Transmission With Soliton Microcombs," *J. Light. Technol.*, vol. 39, no. 13, pp. 4367-4373, Apr. 2021, doi: 10.1109/JLT.2021.3073567.

[17] J. Wu, X. Xu, T. G. Nguyen, S. T. Chu, B. E. Little, R. Morandotti, A. Mitchell, and D. J. Moss, "RF Photonics: An Optical Microcombs' Perspective," *IEEE J. Sel. Top. Quantum Electron.*, vol. 24, no. 4, pp. 6101020, Feb. 2018, doi: 10.1109/JSTQE.2018.2805814.

[18] M. Suh, X. Yi, Y. Lai, S. Leifer, I. S. Grudinin, G. Vasisht, E. C. Martin, M. P. Fitzgerald, G. Doppmann, J. Wang, D. Mawet, S. B. Papp, S. A. Diddams, C. Beichman, and K. Vahala, "Searching for exoplanets using a microresonator astrocomb," *Nat. Photonics*, vol. 13, pp. 25-30, Jan. 2019, doi: 10.1038/s41566-018-0312-3.

[19] Z. Gong, et al., "Soliton microcomb generation at 2 mu m in z-cut lithium niobate microring resonators," *Opt. Lett.*, vol. 44, no. 12, pp. 3182-3185, Jun. 2019, doi: 10.1364/OL.44.003182.

[20] X. Lu, S. Rogers, W. C. Jiang and Q. Lin, "Selective engineering of cavity resonance for frequency matching in optical parametric processes," *Appl. Phys. Lett.*, vol. 105, pp. 1-5, Oct. 2014, doi: 10.1063/1.4898001.

[21] X. Lu, A. Rao, G. Moille, D. A. Westly and K. Srinivasan, "A universal frequency engineering tool for microcavity nonlinear optics: multiple selective mode splitting of whispering-gallery resonances," *Photonics Res.*, vol. 8, no. 11, pp. 1676-1686, Nov. 2020, doi: 10.1364/PRJ.401755.

[22] S. Yu, D. C. Cole, H. Jung, G. T. Moille, K. Srinivasan and S. B. Papp, "Spontaneous pulse formation in edgeless photonic crystal resonators," *Nat. Photonics*, vol. 15, pp. 461-467, Jun. 2021, doi: 10.1038/s41566-021-00800-3.

[23] S. Yu, E. Lucas, J. Zang and S. B. Papp, "A continuum of bright and dark-pulse states in a photonic-crystal resonator," *Nat. Commun.*, vol. 13, no. 3134, pp. 1-10, Jun. 2022, doi: 10.1038/s41467-022-30774-x.

[24] X. Lu, A. McClung and K. Srinivasan, "High-Q slow light and its localization in a photonic crystal microring," *Nat. Photonics*, vol. 16, pp. 66-71, Jan. 2022, doi: 10.1038/s41566-021-00912-w.

[25] X. Lu, et al., "Rod and slit photonic crystal microrings for on-chip cavity quantum electrodynamics," *Nanophotonics*, vol. 12, no. 3, pp. 1-9, Jan. 2023, doi: 10.1515/nanoph-2022-0622.

[26] G. Moille, X. Lu, J. Stone, D. Westly and K. Srinivasan, "Arbitrary Microring Dispersion Engineering for Ultrabroad Frequency Combs: Photonic Crystal Microring Design Based on Fourier Synthesis," 2022, arXiv:2210.14108v1.

[27] W. Bogaerts and L. Chrostowski, "Silicon Photonics Circuit Design: Methods, Tools and Challenges," *Laser Photonics Rev.*, vol. 12, no. 4, pp. 1-29, Mar. 2018, doi: 10.1002/lpor.201700237.

[28] S. Y. Siew, et al., "Review of Silicon Photonics Technology and Platform Development," *J. Light. Technol.*, vol. 39, no. 13, pp. 4374-4389, Jul. 2021, doi: 10.1109/JLT.2021.3066203.

[29] A. G. Griffith, et al., "Silicon-chip mid-infrared frequency comb generation," *Nat. Commun.*, vol. 6, no. 6299, pp. 1-5, Feb. 2015, doi: 10.1038/ncomms7299.

[30] S. Coen, H. G. Randle, T. Sylvestre and M. Erkintalo, "Modeling of octave-spanning Kerr frequency combs using a generalized mean-field Lugiato-Lefever model," *Opt. Lett.*, vol. 38, no. 1, pp. 37-39, Dec. 2012, doi: 10.1364/OL.38.000037.

[31] A. B. Salem, R. Cherif and M. Zghal, "Raman Response of a Highly Nonlinear As2Se3-based Chalcogenide Photonic Crystal Fiber," in *PIERS Proceedings*, Marrakesh, Morocco, 2011, pp. 1256-1260.

[32] J. M. Dudley, G. Genty and S. Coen, "Supercontinuum generation in photonic crystal fiber," *Rev. Mod. Phys.*, vol. 78, pp. 1135-1184, Oct. 2006, doi: 10.1103/RevModPhys.78.1135.

[33] G. P. Agrawal, "Supercontinuum Generation," in *Nonlinear Fiber Optics*, 5th ed. London, Great Britain: ELSEVIER, 2013, pp. 566-570.

[34] H. Jung and H. X. Tang, "Aluminum nitride as nonlinear optical material for on-chip frequency comb generation and frequency conversion," *Nanophotonics*, vol. 5, no. 2, pp. 263-271, Jun. 2016, doi: 10.1515/nanoph-2016-0020.

[35] X. Liu, A. W. Bruch and H. X. Tang, "Aluminum nitride photonic integrated circuits: from piezo-optomechanics to nonlinear optics," *Adv. Opt. Photonics*, vol. 15, no. 1, pp. 236-317, Mar. 2023, doi: 10.1364/AOP.479017.

[36] X. Liu, et al., "Integrated High-Q Crystalline AlN Microresonators for Broadband Kerr and Raman Frequency Combs," *ACS Photonics*, vol. 5, no. 5, pp. 1943-1950, Apr. 2018, doi: 10.1021/acsphotonics.7b01254.

Zongxing Lin received the B.S. degree from the Xidian University, Xi'an, China, in 2019. He is currently working toward the Ph.D. degree at the Zhejiang University, Hangzhou, China. His research interests include high-performance passive devices, supercontinuum generation, Kerr frequency comb generation, dissipative Kerr soliton, and nonlinear dynamics in microresonators on the platforms of silicon-on-insulator (SOI), silicon nitride (SiN), and lithium-niobate-on-insulator (LNOI).

Dongmei Huang received the B.S. degree from the Huazhong University of Science and Technology, Wuhan, China, in 2014, the M.S. degree from Chongqing University, Chongqing, China, in 2017, and the Ph.D. degree from The Hong Kong Polytechnic University, Hong Kong, in 2020. She is currently an Assistant Professor with Photonics Research Institute, The Hong Kong Polytechnic University. Her research interests include wavelength swept lasers and its applications in optical coherence tomography and optical sensing systems, and nonlinear microresonators.

Zihao Cheng received the B.S. degree from the Peking University, Beijing, China, in 2014, the M.S. degree from the Peking University, Beijing, China, in 2017, and the Ph.D. degree from The Hong Kong Polytechnic University, Hong Kong, in 2022. His research interests include integrated optics, silicon photonics, and nonlinear microresonators.

Wei Wu received the B.S. degree from the Dalian University, Dalian, China, in 2016, and the Ph.D. degree from Xi'an Institute of Optics and Precision Mechanics (XIOPM), Chinese Academy of Sciences, Beijing, China, in 2022. He is currently a postdoctoral fellow at Photonics Research Institute of The Hong Kong Polytechnic University. His current research interests include planar waveguide and devices, Kerr optical frequency comb, and nonlinear optics.

P. K. A. Wai (Fellow, IEEE) received the B.S. (Hons.) degree from The University of Hong Kong, Hong Kong, in 1981, and the M.S. and the Ph.D. degrees from the University of Maryland, College Park, MD, USA, in 1985 and 1988, respectively. In 1988, he joined Science Applications International Corporation, McLean, VA, USA. In 1990, he was a Research Associate at the University of Maryland. In 1996, he joined the Department of Electronics and Information Engineering, The Hong Kong Polytechnic University, Hong Kong. In 2005, he was a Chair Professor of Optical Communications. Currently, he is the Chair Professor of Photonics in Hong Kong Baptist University. He is an active contributor to the field of photonics and optical communications. He has authored or coauthored more than 300 international refereed publications. His research interests include soliton, fiber lasers, modeling and simulations of optical devices, long-haul optical fiber communications, all-optical packet switching, and network theories. He is also a Fellow of OSA.

Zhe Kang received the B.S. degree from the Wuhan University of Technology, Wuhan, China, in 2006, the M.S. degree from Dalian Polytechnic University, Dalian, China, in 2012, and the Ph.D. degree from the Beijing University of Posts and Telecommunications, Beijing, China, in 2015. From 2015 to 2019, he joined the Department of Electronics and Instrumentation Engineering, The Hong Kong Polytechnic University, Hong Kong, as a Postdoctoral Fellow. He is currently an Assistant Professor with COER and NRI, Zhejiang University, Hangzhou, China. His research interests include nonlinear fiber optics, nonlinear silicon photonics, and nonlinear dynamics in optical devices and optical systems, especially supercontinuum generation, Kerr frequency comb in microresonators, dissipative Kerr soliton, mode-locked fiber lasers, and nonlinear pulse shaping.

Sailing He (Fellow, IEEE) received the Licentiate of Technology and the Ph.D. degrees in electromagnetic theory from the KTH Royal Institute of Technology, Stockholm, Sweden, in 1991 and 1992, respectively. Since then, he has been with the KTH Royal Institute of Technology, as an Assistant Professor, an Associate Professor, and a Full Professor. He is currently a Professor with Zhejiang University (ZJU), Hangzhou, China and is currently the Director with the KTH-ZJU Joint Research Centre of Photonics, China. He has first-authored one monograph (Oxford University Press) and authored or coauthored more than 700 papers in refereed international journals. His current research interests include sub-wavelength photonics, sensing technologies, optical communication, and applied electromagnetics. He is also a Fellow of OSA, SPIE, and The Electromagnetics Academy.